Computational Methods and Experimental Measurements VIII

Editors:
P. Anagnostopoulos,
G.M. Carlomagno,
C.A. Brebbia

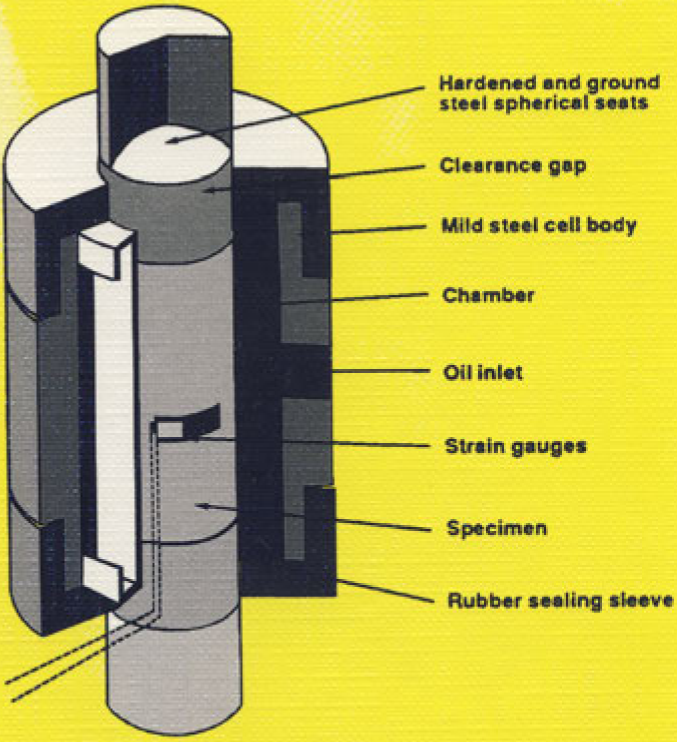

Computational Mechanics Publications

Computational Methods and Experimental Measurements

EDITORS:

P. Anagnostopoulos
University of Thessaloniki, Greece

G.M. Carlomagno
University of Naples, Italy

C.A. Brebbia
Wessex Institute of Technology

Computational Mechanics Publications
Southampton, UK and Boston, USA

CONTENTS

Section 1: Stress Analysis

An efficient data processing scheme for the analysis of in-situ stresses in concrete structures 3
D W Begg, W Huang, A Owens

An analysis of stress and strain state in freight car wheels 15
A Sladkovsky, V Yessaulov, N Shmurygin, Y Taran, S Gubenko

Experimental verification of folded glass plates used in architectural window glazing 25
C V G Vallabhan, M M El-Shami, K S Kandil, O M Tawfik

Layout optimisation by photoelastic technique and by finite element analysis 35
D Tran, M Xie, T Do

Various experimental applications of digital image correlation method 45
S Mguil-Touchal, F Morestin, M Brunet

A comparison between actual displacements and numerical results from a finite element model in an arch dam 59
L E Romera, S Hernández

Estimation of plastic deformation in strain rate dependence materials by infrared video system 67
H Sakamoto

Nonlinear numerical analysis and computer control of pipe denting experiments 77
R Rajagopalan, S G Ladkany

Finite element simulation and on plant experimental validation of sheet metal forming 87
M McLennan, M Cardew-Hall, R Taube

Endochronic material modelling in nonlinear FE-analysis of folded plates 97
B Möller, W Graf, J Kluger

An Analysis of Stress and Strain State in Freight Car Wheels

A.Sladkovsky, V.Yessaulov, N.Shmurygin, Y.Taran & S.Gubenko
State Metallurgical Academy
Prospekt Gagarina, 4, Dnepropetrovsk, 320635, Ukraine
Email: dmeti@dmeti.dnepropetrovsk.ua

Abstract

A semianalytical finite element method was employed for analysis of railroad car wheels. The accuracy of the computational model was estimated by comparing the numerical results with analytical solutions for a simplified wheel model and with tensometric data. Innovative wheel designs were developed and subjected to full-scale tests. The wheels were rolled following computer-assisted engineering of the new designs. Their advantages over conventional wheels were validated by operational tests.

1 Introduction

Designing railroad car wheels necessarily involves analysis of the state of stress and strain in appropriate models. Clearly, a wheel in service is subjected to a great multitude of diverse external factors of mechanical and/or thermal nature. The problems thus arising are solved by numerical methods of mechanics of deformable solids. Finite element method (FEM) is a most effective technique for such tasks. For a check of their reliability, however, the numerical results must be compared with analytical trial solutions and experimental data.

A semianalytical FEM technique was mainly used for the numerical analysis of the state of stress in wheels in this study. Solutions obtained by complex analysis of simplified wheel models were employed to estimate the overall computation scheme and errors introduced by the finite element quantization. The comparison also included distributions of strain and temperature generated in laboratory tensometric tests on model wheels.

Full-scale tests under operational conditions involved both tensometric measurements and microstructure characterization.

2 Investigation of the state of stress in wheels

The problem statement for the state of stress in railroad car wheels was presented previously [1]. Here, the focus is on the accuracy of solutions. This issue is of considerable importance, although it has not received sufficient attention in some applied research papers thus giving errors ranging from 20 to 150 %. Figure 1 depicts a finite element mesh for quantization of a radial section of a railroad wheel. The utilization of Fourier series for all vectors involved in the analysis of stress, namely mesh point displacements, strains, and stresses, permits a three-dimensional presentation and thus enables determination of stresses in any radial section. A side task is to determine the desirable numbers of Fourier series terms.

Figure 2 shows a wheel model having a planar plate of constant thickness. This type of running wheel is used in traveling cranes. The rigidity of the plate is much lower than that of the hub or the rim. For purposes of strain analysis, the plate (confined between the thick lines in Fig. 2) can therefore be regarded to be rigidly fixed along these contours; furthermore, the inner plate (hub) contour L_1 is considered to be stationary while the outer (rim) contour L_2 is rotatable and allows displacement.

The elastic version of problem statement adopted permitted superposition of solutions for the problems of (1) plane deformation of the plate due to the vertical force P, (2) flat torsion due to the force T opposing rolling, (3) axisymmetric bend of the plate, and (4) torque-induced bend of the plate. Problems 3 and 4 stem from the fact that for the region at hand the impact of a lateral force Q applied to the flange can be represented by stresses applied to the outer contour and described by a principal vector Q and a principal torque M equal to a product of Q by the radial position R_0 of the force point.

Consider problem 1. Under the force P applied to it, the contour L_2 undergoes an unknown parallel displacement Δ (depression of the wheel). Problem 2 for a circular ring is stated after Muskhelishvili [2], i.e. for the entire boundary $L = L_1 \cup L_2$ the boundary conditions are given in terms of displacements, and complex valued functions φ and ψ are sought which are dependent on the complex valued variable $z = x + iy = re^{i\theta}$ and for which the following condition is given at L:

$$\chi\varphi(z) - \overline{z\varphi'(z)} - \overline{\psi(z)} = 2\mu(g_1 + ig_2) \tag{1}$$

Here, the parameters μ and χ for a generalized plane state of stress are defined as

$$\mu = \frac{E}{2(1+\nu)}, \quad \chi = \frac{3-\nu}{1+\nu} \tag{2}$$

where E is the modulus of elasticity and ν the Poissons ratio of the wheel material. The cross bars in Eq. (1) relate to conjugation. For the problem at hand, the functions g_i are

$$g_1 = 0 \quad , \qquad g_2 = 0 \qquad \text{at } L_1 \tag{3}$$

$$g_1 = 0 \quad , \qquad g_2 = \Delta \qquad \text{at } L_2 \tag{4}$$

Due to double connectivity of the region under consideration, the solution is sought in the form

$$\varphi(z) = \gamma_1 \ln z + \sum_{-\infty}^{\infty} a_k z^k \tag{5}$$

$$\psi(z) = \gamma_1' \ln z + \sum_{-\infty}^{\infty} a_k' z^k \tag{6}$$

Substituting Eqs. (5) and (6) to the boundary conditions (1), (3) and (4) and equating the coefficients of θ and $e^{i\theta k}$ to zero, one obtains the coefficients in the series. The final expressions for φ and ψ are

$$\varphi(z) = \frac{\mu\Delta}{c}\left[\chi\left(R_1^2 + R_2^2\right)\ln z + z^2\right] \tag{7}$$

$$\psi(z) = \frac{\mu\Delta}{c}\left[-\chi^2\left(R_1^2 + R_2^2\right)\ln z + 2\chi^2\left(R_1^2 + R_2^2\right)\ln R_1 - \right.$$
$$\left. -2R_1^2 - \frac{\chi R_1^2 R_2^2}{z^2}\right] \tag{8}$$

$$c = R_1^2 - R_2^2 - \chi^2\left(R_1^2 + R_2^2\right)\ln\frac{R_1}{R_2} \tag{9}$$

Here R_1, R_2 are the plate radii at the hub and the rim respectively. Substitution of φ and ψ into the Muskhelishvili equations

$$\sigma_r + \sigma_\theta = 2\left[\varphi'(z) + \overline{\psi'(z)}\right] \tag{10}$$

$$\sigma_r - \sigma_\theta + 2i\tau_{r\theta} = 2\left[\bar{z}\varphi''(z) + \psi'(z)\right]e^{2i\theta} \tag{11}$$

gives the radial σ_r and the hoop σ_θ .normal stresses as well as the tangential stresses $\tau_{r\theta}$ at the plate side,

$$\sigma_r = \frac{\mu\Delta}{c}\left[3\frac{\chi\left(R_1^2 + R_2^2\right)}{r} + 2r + \frac{\chi^2\left(R_1^2 + R_2^2\right)}{r} - 2\chi R_1^2 R_2^2 \frac{1}{r^3}\right]\cos\theta \tag{12}$$

$$\sigma_\theta = \frac{\mu\Delta}{c}\left[\frac{\chi\left(R_1^2 + R_2^2\right)}{r} + 6r - \frac{\chi^2\left(R_1^2 + R_2^2\right)}{r} + 2\chi R_1^2 R_2^2 \frac{1}{r^3}\right]\cos\theta \tag{13}$$

$$\tau_{r\theta} = \frac{\mu\Delta}{c}\left[\frac{\chi\left(R_1^2 + R_2^2\right)}{r} + 2r - \frac{\chi^2\left(R_1^2 + R_2^2\right)}{r} - 2\chi R_1^2 R_2^2 \frac{1}{r^3}\right]\sin\theta \tag{14}$$

The displacement Δ can be found from the equilibrium condition,

$$\Delta = \frac{cP}{2\mu\pi(1 + \chi)\chi\left(R_1^2 + R_2^2\right)h} \tag{15}$$

h being the plate thickness.

A similar approach was used for problem 2. Let the force opposing rolling or the tractive force generate a torque of $M_k = TR$, R being the tread radius. The outer contour will then be rotated with respect to the inner contour through an angle ζ (the angle of plate rotation). The functions $g_i(z)$ for L_1 can then be written in the form of Eq. (3) while

$$g_1 = -R_2\zeta \sin\theta \quad , \qquad g_2 = R_2\zeta\cos\theta \qquad \text{at } L_2 \tag{16}$$

Substituting (5) and (6) into the boundary conditions, one finds the functions φ and ψ.

$$\varphi(z) = \frac{2\mu R_2^2 \zeta i z}{(\chi+1)\left(R_2^2 - R_1^2\right)} \tag{17}$$

$$\psi(z) = -\frac{2\mu R_1^2 R_2^2 \zeta i}{\left(R_2^2 - R_1^2\right)z} \tag{18}$$

where the angle ζ is defined as

$$\zeta = \frac{M_k\left(R_2^2 - R_1^2\right)}{4\pi\mu R_1^2 R_2^2 h} \tag{19}$$

Problems 3 and 4 were solved in a similar manner using relationships of Savin and Fleishman [3]. Figure 3 provides examples of how the stresses σ_r, σ_θ, $\tau_{r\theta}$ are distributed at the sides of vertical plate section. Actual service data were taken for the wheel characteristics and load values, namely P = 129 kN, Q = 1.47 kN, T = 4.7 kN, R = 250 mm, R_1 = 122.5 mm, R_2 = 176.7 mm, R_0 = 262.5 mm.

To estimate the error resulting from the finite element quantization, various grids were used in the semianalytical FEM technique for the problem at hand. It was found that the error is at its maximum when the plate is bent. Consider the zeroth harmonic for a bent plate whose inner and outer contours are rigidly fixed while the outer contour allows an axial displacement under an axial load, so that an axisymmetric flexure occurs in the plate. Assume a maximum deflection of the plate at $\Delta_z = 0.01$ cm. The above solution procedure yields the axial force Q:

$$Q = \frac{8\pi D\Delta_z}{R_2^2\left(\dfrac{\eta^2+1}{2\eta^2} - \dfrac{1}{\eta^2} - \dfrac{2\ln^2\eta}{\eta^2-1}\right)} \tag{20}$$

where $D = \dfrac{Eh^3}{12\left(1-\nu^2\right)}$, $\eta = \dfrac{R_2}{R_1}$. Substituting numerical values into Eq. (20) yields an exact value of Q = 19.307 kN. Table 1 lists values of Q found by the FEM technique and their relative errors for a variety of meshes. The number of mesh points in the plate equals $N = n_h \times n_r$, n_h and n_r being the mesh point number across the plate thickness and the plate radius respectively.

Clearly, the error is large at small numbers of mesh points across the plate thickness. Optimum mesh should be found on a case-by-case basis to minimize the calculation error. The limitations will be imposed by the available computer working storage WS given in the right-hand column, and the processing time. To allow for various computer speeds, the table lists TR, the ratio of computation time for a given mesh to that for the 5×10 mesh. It was found that with an optimum 10×80 mesh the calculation error for a freight car wheel is within 5 %. The Fourier expansion then must have at least 11 terms.

Table 1. Influence of mesh on the accuracy of FEM solution for the problem of flexure of a plane wheel plate

n_k	n_r	Q, kN	δ_Q , %	TR	WS, kbyte
5	10	56.15	190.8	1.0	128
5	20	29.87	54.71	2.0	128
5	40	23.81	23.34	4.24	256
5	80	22.34	15.73	8.84	384
10	10	54.12	180.1	2.84	256
10	20	27.68	43.39	6.8	384
10	40	21.56	11.72	11.08	704
10	80	20.07	3.954	20.96	1344
15	10	53.87	179.0	5.32	384
15	20	27.41	41.97	14.24	768
15	40	21.27	10.20	21.08	1472
15	80	19.71	2.127	46.04	2816

3 Experimental

Laboratory experiments were carried out on 1:4 scale model wheels. The models were made from wheel steel forgings using specially made outline templates to check wheel shape. A pair of wheels was then press-mounted on an axle having shoulders at its ends to transmit vertical loads.

A finished wheelset was tested in a special rig shown in Fig. 3. The equipment included a 0.5 MN hydraulic press **1**. The top cross-rail carried a beam **2** with vertical load cells **3** and axle boxes **4** that transferred vertical loads to the axle necks. The bottom cross-rail **5** supported simulator rails **6**, hydraulic cylinders generating a lateral force, and lateral load cells **7**. A hand-power press and a manometer **8** for measuring the pressure in the lateral hydraulic cylinders were mounted on a side support. To simulate thermal effects of braking, an induction heater **9** was provided that included a thermally insulated heating element encapsulated in a brass housing which surrounded the tread and was brought in close contact with it via a spring clamp. The heating rates were selected in a manner permitting simulation of temperature gradients developing in a wheel at various braking modes.

The vertical loads developed by the press **1** were monitored visually using the control panel **10**. The distribution of the vertical load between the two wheels was checked by the use of the vertical load cells **3**. The rim temperature was measured with thermocouples fixed to the wheels. Radial and hoop strain gages were bonded to the model wheel **11**. The signals were processed by the measuring and recording unit **12**.

The experimental loads were selected based on operational data and the similarity theory. For example, a vertical load of 31.2 kN in the laboratory tests corresponded to an actual axle load of 500 kN. From the measured strain distributions, stresses at the wheel sides were calculated. These were compared with the estimated results. The experimental and the theoretical data agreed fairly well, within 20 %.

Wheels of various designs were also subjected to full-scale tests under service conditions. These tests were conducted on wheelsets provided with strain gages and thermocouples. The car speed, the vertical load and the wheel diameter were varied in the tests. In braking tests, braking modes also were set. The state of stress and strain in wheel plates, the vertical and the lateral load, and the temperature distribution were recorded. The static load was 0.24 MN per axle. The running speed ranged from 20 to 80 km/h. The sensor signals were taken via special mercury current collectors mounted at an axle end. The tests yielded distributions of static and dynamic stresses alike. The theoretical and experimental data made a basis for development of novel wheel designs featuring reduced wear, improved reliability and extended service life.

4 Wheel material characterization

Microstructural changes in the actual wheel material regions adjoining the tread having a conventional or a curvilinear profile were investigated for comparison with the data of mathematical simulation of wheel-rail contact interaction. In service, the tread undergoes severe wear associated with mechanical stresses developing in the contact areas as well as with thermal stresses caused by braking. The stress values are functions of elastic constants of the rail and the wheel materials, car running speed, tread surface geometry etc. The microstructural changes near tread surface are mainly manifested by occurrence of plastic shear regions with elongated grains, Fig. 4a, and white layers composed of cryptocrystalline martensite, Fig. 4b. Note that in service the tread changes its profile due to bulge formation as a result of metal flow from the tread middle towards the rim outer side.

For various tread profiles, the grain relative elongation ε, the plastic shear depth h and the dislocation density $\rho_\perp$ were determined, see Table 2. The conventional-tread-profile wheels displayed more rapid wear rate than those having a curvilinear tread profile. This is associated with differences in contact stresses σ as shown in Table 2. Three wheel regions were characterized, namely the transition to flange (A), the middle portion of tread (B), and the bulged metal region (C).

It should be noted that the thermal stresses resulting from quenching and tempering in an as-made wheel are supplemented by microstructural stresses due to existence of grain boundaries, interfaces, and nonmetallic inclusions responsible for long-range stress fields. Electron microscopy was used to study these stresses. Following bend twist tensors (dislocation densities) were obtained that normally have one or two nonzero components:

- ferrite/cementite interface:

$$\chi = \begin{vmatrix} 0 & 0 & 0 \\ 710 & 0 & 710 \\ 0 & 0 & 0 \end{vmatrix}, \text{ rad/cm} \qquad (21)$$

- nonmetallic (Al_2O_3) inclusion/ferrite matrix:

$$\chi = \begin{vmatrix} 0 & 0 & 0 \\ 848 & 0 & 0 \\ 0 & 0 & 0 \end{vmatrix}, \text{ rad/cm} \qquad (22)$$

Table 2. Microstructural characteristics of used wheel steel near the tread surface. 1, conventional tread profile; 2, curvilinear tread profile; A, B, C: measurement regions

	ε, %			h, mm			$\rho_\perp$, cm^{-2}			σ, MPa	
	A	B	C	A	B	C	A	B	C	A	B
1	65-75	22-25	90	300	30	600	$9.22 \cdot 10^{11}$	$3.73 \cdot 10^{9}$	$9.6 \cdot 10^{10}$	1350	1250
2	60-70	10	80	180	20-40	420	$6.54 \cdot 10^{10}$	$6.41 \cdot 10^{9}$	$8.06 \cdot 10^{11}$	1150	900

The above example values are given for a distance of 1 μm from the interface of the inclusion. The long-range stresses gradually decrease with increasing distance, the range being 2 to 3 times the interface width and 4 to 5 times the inclusion size. The wider the interface or the larger the inclusion, the greater the maximum stress σ_g and the field range radius R_{σ_g}, see Table 3.

The strain-induced stresses make the extinction contour patterns more complex, giving rise to more nonzero tensor components. This means that the lattice bend twist near an interface or an inclusion becomes more intricate due to an excessive dislocation density, e.g.

$$\chi = \begin{vmatrix} 420 & 240 & 240 \\ 0 & 836 & 0 \\ 0 & 0 & 420 \end{vmatrix}, \text{ rad/cm} \qquad (23)$$

The strain-induced stresses increase the values of σ_g and R_{σ_g} near interfaces and inclusions. The long-range stresses make considerable contributions to flow stresses in steel. They cannot be classified with substructure elements but represent a specific hardening factor.

Thus a comprehensive study of freight car wheels was carried out using numerical and experimental methods. The satisfactory agreement between the theory and the experiment made a good basis for development of new wheel designs.

Table 3. Stress field characteristics near metallurgical defects

Defect type	Defect size, µm	σ_g , MPa	R_{σ_g} , µm
Ferrite/cementite interface	4	1020	7.9
	6	1110	12.8
Al_2O_3 inclusion	5	1020	20.3
	12	1170	49.7
	20	1290	81.3

References

1. Yessaulov, V., Taran, Y., Sladkovsky, A., Kozlovsky, A. & Shmurygin N. Design of wagon wheels using the finite element method, *Computers in Railways V*, Vol.2, pp 69-77, Computational Mechanics Publications, Southampton & Boston, 1996.
2. Muskhelishvili, N.I., *Some principal problems of mathematical theory of elasticity*, Nauka Publishing House, Moscow, 1966. In Russian.
3. Savin, G.N. and Fleishman, N.P., *Plates and shells with stiffening ribs*, Naukova Dumka Publishing House, Kiev, 1964. In Russian.

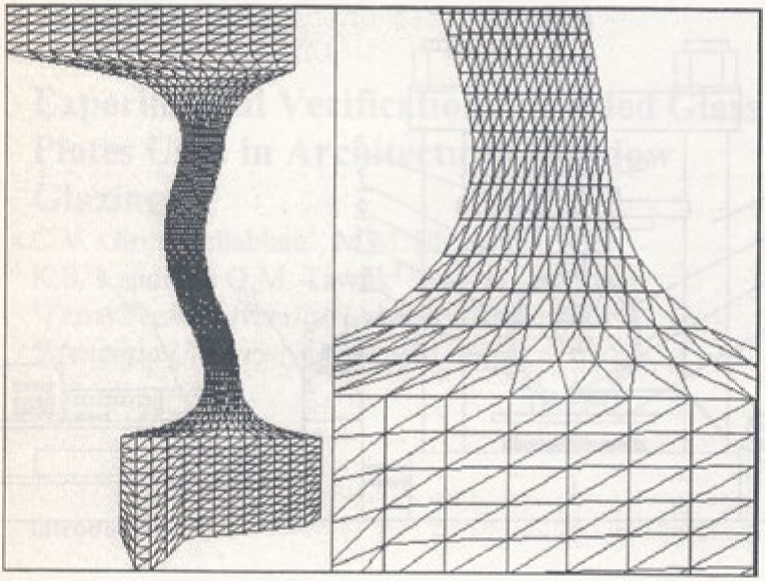

Figure 1. Finite element mesh for a radial section of a freight car wheel. Right: transition from the plate to the rim shown on a larger scale

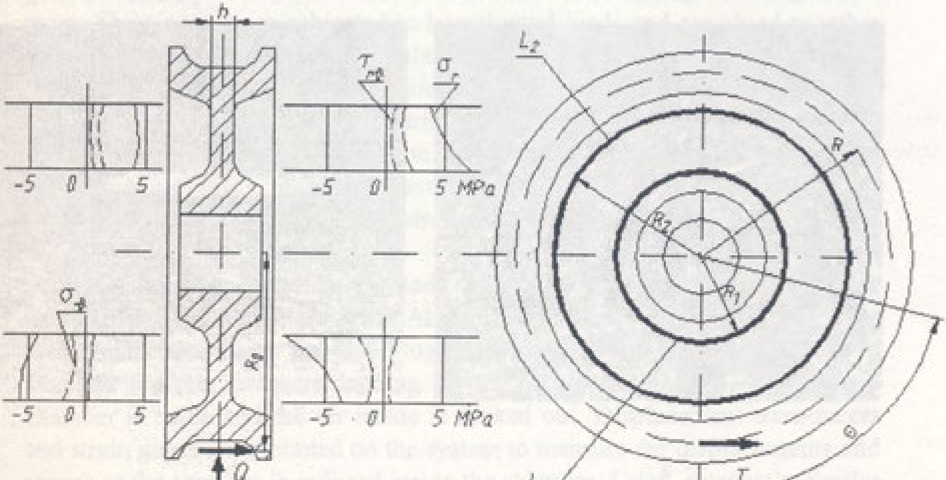

Figure 2. Loading conditions and stress distribution in a vertical section of a constant-thickness plane plate wheel

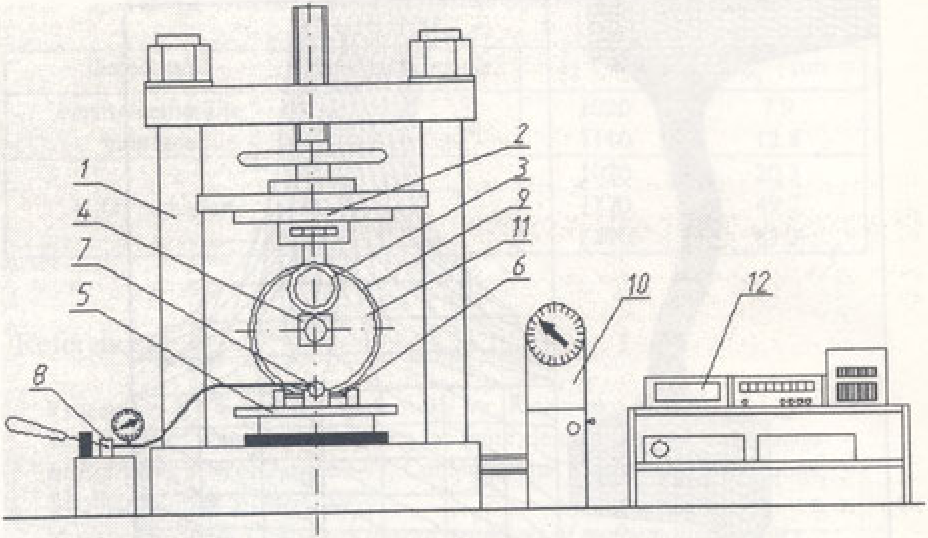

Figure 3. Experimental setup for strain gage measurements of the state of strain and stress in wheels

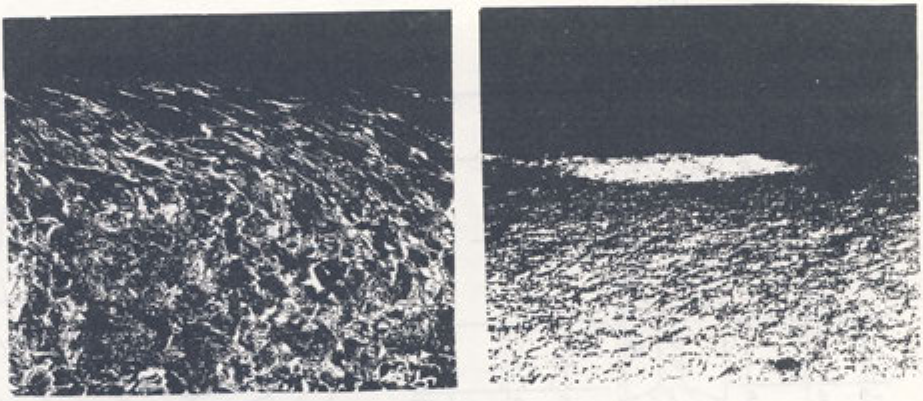

a

b

Figure 4. Microstructure of wheel steel near tread surface. 100×.